Vacuum 227 (2024) 113447

Contents lists available at ScienceDirect

Vacuum

journal homepage: www.elsevier.com/locate/vacuum

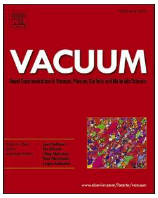

Effects of highly-textured and untextured polycrystalline layers on deformation mechanisms in amorphous submicron-layered materials

Hang Xu [a], Xiao-Ye Zhou [b,**], Jingwen Qiu [c], Tao Guo [a], Kewei Gao [a], Alex A. Volinsky [d], Xiaolu Pang [a,e,*]

[a] School of Materials Science and Engineering, University of Science and Technology Beijing, Beijing, 100083, China
[b] Department of Materials Science and Technology, Shenzhen MSU-BIT University, Shenzhen, Guangdong, 518060, China
[c] School o F Materials Science and Engineering, Hunan University of Science and Technology, Xiangtan, Hunan, 411201, China
[d] Department of Mechanical Engineering, University of South Florida, 4202 E. Fowler Ave. ENG030, Tampa, 33620, USA
[e] Beijing Advanced Innovation Center for Materials Genome Engineering, University of Science and Technology Beijing, Beijing, 100083, China

ARTICLE INFO

Keywords:
Amorphous/crystalline multilayers
Highly-textured crystalline layer
Strain hardening
Homogeneous flow
Free volume

ABSTRACT

Amorphous alloys have high strength, but softening can lead to room temperature brittleness, limiting their applications. Typically, soft means low hardness and yield strength, and the lower the yield stress, the higher the fracture toughness. Two amorphous/crystalline multilayer samples with submicron single layer thickness were prepared. The crystalline layer of one sample is composed of highly-textured (111) nanocrystalline grains, and the other sample is untextured. Indentation experiments proved that the samples were plastically deformed, while the amorphous layer did not form shear bands with decreased layer thickness. The thickness reduction of the amorphous layer in the sample with highly-textured crystalline layers is greater than in the sample with untextured crystalline layers. The strain-hardening ability of the textured crystalline layer is higher, while the corresponding amorphous layer is deformed more severely with free volume annihilation and greater flow with more compact atoms. The amorphous layer corresponding to the untextured crystalline layer absorbs dislocations, and activates shear transformation zones (STZs), increasing the free volume near the interface. The annihilation of the free volume is less than the sample with highly-textured crystalline layers.

1. Introduction

Amorphous alloys, also known as metallic glasses, have the characteristics of long-range disorder and short-range order. They lack typical defects found in crystalline materials, such as dislocations and grain boundaries, and have unique physical, chemical, and mechanical properties [1–3]. These properties include high strength and hardness [4], good wear and corrosion resistance [5–7], excellent soft magnetic properties [8,9], and unique catalytic properties [10], etc. They have been utilized in medicine, sports, catalysis, electronics, and aerospace, and have even broader potential applications [5,11,12]. However, failures caused by rapid expansion of the amorphous alloy shear bands is an Achilles heel, restricting the development of amorphous alloys. One way of overcoming this problem is to combine brittle amorphous phase with ductile crystalline phase to form amorphous/crystalline multilayer structure [13–21]. Amorphous/crystalline multilayer materials have been applied in different fields and at different scales [22–25] by adjusting layer thickness [26] or increasing the constraint of the crystal [20] to suppress the nucleation and propagation of amorphous shear bands, exhibiting good strength and ductility.

Multiple papers have reported the size effects in the amorphous/crystalline layered system and studied the influence of amorphous or crystalline layer thickness on the overall deformation [19,27–29]. The amorphous layer plays the role of absorbing dislocations generated by the crystalline layer at the nanometer scale [13]. Nanometer-sized amorphous phase serves as a high-capacity dislocation sink, avoiding dislocation accumulation [24]. The amorphous/crystalline interface (ACI) acts as a barrier for dislocation movement. As a result, dislocation structures near ACIs are disrupted and dissolved, avoiding large stress concentrations [13]. Nanoscale amorphous layers offer great advantages in improving the strength and plasticity of amorphous/crystalline multilayer structures. Due to this discovery, several nanometers thick

---

* Corresponding author. School of Materials Science and Engineering, University of Science and Technology Beijing, Beijing, 100083, China.
** Corresponding author.
E-mail addresses: xiaoye_zhou@smbu.edu.cn (X.-Y. Zhou), pangxl@mater.ustb.edu.cn (X. Pang).

https://doi.org/10.1016/j.vacuum.2024.113447
Received 4 February 2024; Received in revised form 29 June 2024; Accepted 3 July 2024

amorphous films are used in crystalline materials, where nucleation and propagation of cracks are delayed [30,31]. When the thickness of the amorphous layer exceeds 100 nm, it is easy to form the main shear band and cause overall damage. This situation can be improved by adjusting the thickness ratio of the amorphous and crystalline layers [32].

In addition to the size effect on the amorphous/crystalline layered structure, molecular dynamics (MD) simulations show that the crystal orientation affects amorphous deformation. Song et al. [33] used MD simulations to demonstrate that the plastic deformation mechanism of the amorphous nanocrystalline laminates depends not only on the thickness of the amorphous phase but also on the orientation of the crystalline phase. Local deformation dominated by the generalized shear band (GSB) transformed into uniform plastic deformation with the change of the amorphous layer thickness in the first orientation model. In the other orientation model, no matter how the amorphous thickness changed, the local plastic deformation was dominated by GSB. The simulation by Alishahi et al. [34] showed that the yield strength and plasticity of amorphous-crystalline (A-C) composites highly depend on the crystalline layer orientation. When the slip plane in the crystalline layer is well aligned with the shear band in the amorphous layer, strong shear localization will be caused in the crystalline and amorphous layers.

The scale of MD simulations is usually limited to a few or tens of nanometers [33–36]. Meanwhile, due to the difficulty of manufacturing amorphous/crystalline multilayer structures with different orientations, no experiments have been conducted to investigate the effects of crystalline layer orientation on the deformation of amorphous layers. Considering the above two points, amorphous/crystalline multilayer samples with a single submicron layer were prepared by electroplating in this paper. The influence of highly-textured and untextured polycrystals on the deformation mechanism of amorphous layers under indentation was investigated. Experimental results show that the highly-textured crystalline layers are more conducive to the reduction of the amorphous layers thickness. The reasons why highly-textured and untextured crystalline layers have different effects on amorphous reduction were analyzed, combined with the deformation of amorphous/crystalline layers with different orientations using indentation, and demonstrated by MD simulations.

2. Experiment

2.1. Samples preparation

Amorphous/crystalline Ni–P/Ni multilayers were prepared by electrodeposition in a dual bath [37]. Amorphous and crystalline layers are of equal thickness of about 250 nm. The parameters of the amorphous layer electroplating solution were as follows: nickel sulfate 300 g/L, nickel chloride 45 g/L, boric acid 40 g/L, phosphorous acid 20 g/L, and sodium dodecyl sulfate 0.25 g/L. The pH value was 2 ± 0.2 and the temperature was 343 ± 2 K. Applied current density was 30 mA/cm^2. The electroplating solution parameters of crystalline layers of the first sample, marked as Sample #1, are as follows: nickel sulfate 250 g/L, nickel chloride 40 g/L, boric acid 35 g/L, sodium dodecyl sulfate 0.05 g/L, and saccharin 0.8 g/L. The pH value was 4 ± 0.2 and the temperature was 328 ± 2 K. Applied current density was 35 mA/cm^2. The difference between the crystalline plating solution of the second sample marked as Sample #2, and the crystalline plating solution of the first sample is that 1.2 g/L lanthanum chloride was added, and the rest of the parameters were the same as sample #1. After each layer was deposited, the sample was quickly rinsed with deionized water, then ultrasonically cleaned with 10 % sulfuric acid for 1 min, and rinsed again with deionized water to ensure that the sample surface was clean and the sample surface was activated to ensure good bonding between the layers. Two multilayer specimens have an amorphous top layer from which the shear band is expected to initiate. Due to the wear and corrosion resistance of amorphous materials, using the amorphous Ni–P as the top layer can protect the sample. The total thickness of the multilayer is about 4.5 μm.

2.2. Indentation tests

Indentation is a convenient method for deforming amorphous and crystalline layered thin films, avoiding the interaction between the thin film and the substrate in the layered structure [38].

The samples were indented with a 0.5 kgf Vickers indenter for 10 s. After indentation, a pyramid-shaped pit was formed. The cross-section of the amorphous/crystalline multilayers before and after deformation was cut by focused-ion-beam (FIB, Helios G4 CX). After deformation, the cross-section of the specimen was cut at the deepest part of the indent, just below the indenter tip. The ImageJ software was used to measure the thickness of each layer before and after deformation.

2.3. Characterization

The amorphous phase and crystal orientation of the samples were characterized by X-ray diffraction (XRD, Rigaku D/Max 2550X). The microstructure of the two amorphous/crystalline multilayer samples before and after indentation was characterized by scanning electron microscopy (SEM, GeminiSEM 300) and transmission electron microscopy (TEM, JEM-2010).

2.4. MD simulations

The embedded atom method (EAM) developed by Sheng et al. [39] was used to describe the interatomic interactions of the amorphous Ni–P layer and the crystalline Ni. The MD simulations were conducted using the open-source large-scale atomic/molecular massively parallel simulator (LAMMPS). The atomic configurations of the amorphous Ni–P were obtained by quenching a fully melted equimolar Ni–P model from 2000 K down to 1 K. The cooling rate was 10^{-12} K s^{-1}. The single crystal model was constructed by filling the hexagonal grains with a fully relaxed face-center cubic (FCC) Ni. The grains were aligned along the out-of-plane direction. The Ni–P/Ni composite was built by combining the amorphous Ni–P layer with the single crystal Ni layer. The Ni layer is located above Ni–P, and its main purpose is to simulate how crystalline layers with different orientations transfer stress to the amorphous layer, creating a strong constraint on the amorphous layer. The periodic boundary conditions were applied in all directions. Four composite models were built with different orientations of single crystalline grains, namely (111), (220), (112), and (110). Then the composite model was indented with a spherical indenter with a constant rate of 10 m/s at 300 K. During indentation, the outmost part of the composite was fixed while the rest was deformed. The atomic model for the indentation simulation is presented in Fig. 1. Visualization of atomic configurations and dislocations was facilitated by the Open Visualization Tool (OVITO) package [40], with dislocations identified via the DXA module [41] within OVITO.

3. Results

Fig. 2 shows the cross-section of the multilayer and the top view of the amorphous layer. The crystalline and amorphous layers exhibit distinct layered structures with clear interfaces. P content of the Ni–P amorphous layer is ~10.5 wt%. The surface morphology and P content are consistent with the amorphous Ni–P described in the literature [42,43]. The TEM analysis of the two samples is presented in Fig. 3(a and b). The selected area diffraction (SAED) patterns inserted in Fig. 3(a and b) show the amorphous halo of the Ni–P layer of the two samples, which is consistent with the broad diffraction hump of the Ni–P layer in Fig. 3(c), both confirming the amorphous structure of the deposited Ni–P layer. The XRD pattern in Fig. 3(c) shows that the Ni layer of the Sample #1 has a strong (111) texture. In contrast, the Ni layer of the Sample #2,

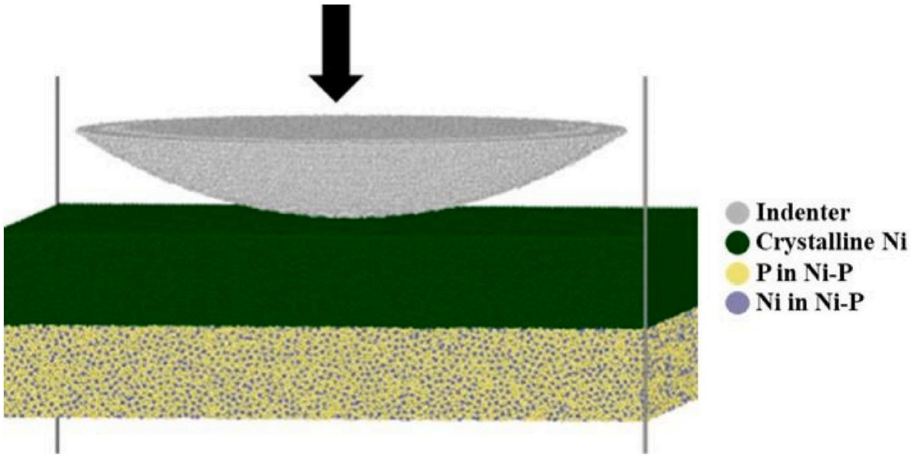

Fig. 1. The atomic model for the indentation simulation.

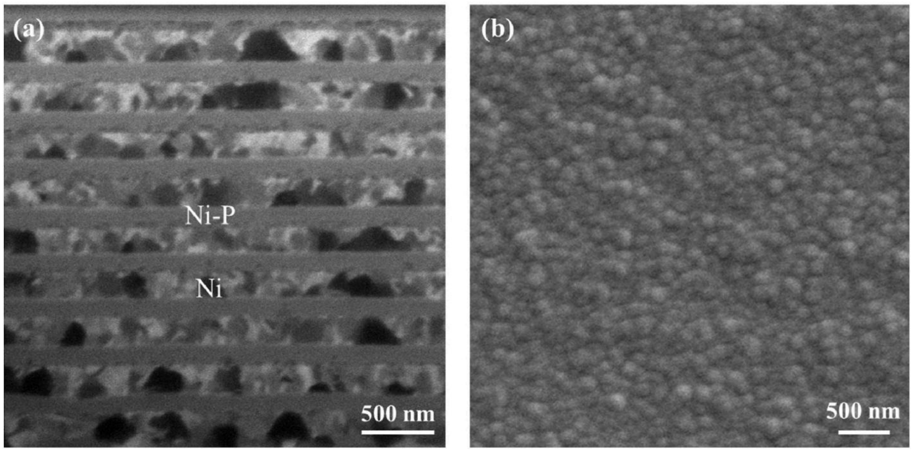

Fig. 2. (a) Cross-section and (b) surface amorphous layer morphology of amorphous/crystalline multilayer samples.

shows (111), (200), and (220) orientations without strong texture. The SAED patterns of all crystalline layers in Samples #1 and #2 were examined, and the intensity distribution was extracted [44], which matched the XRD patterns. Fig. 3(d and e) show the intensity distribution of SAED pattern extraction for crystalline layers of Samples #1 and #2, respectively.

After indentation, the deepest part of the indentation pit was covered with a layer of Pt to protect the FIB cross-section. The cut position is shown in Fig. 4(a). Fig. 4(a and b) shows the cross-section under the indenter of Sample #1, and Fig. 4(b) shows enlargement of Fig. 4(a). Fig. 4(c and d) shows the cross-section of Sample #2, and Fig. 4(d) shows enlargement of Fig. 4(c). The thickness of the amorphous layer decreased after indentation. Compared with Fig. 4(b) and (d), the thickness reduction of the amorphous layer of Sample #1 is larger than Sample #2, while the thickness of the crystalline layer has little difference, so the total thickness of Sample #1 after indentation is less than Sample #2. Three amorphous layers were selected to calculate the transverse thickness of the deformed amorphous layer. The central position under the indenter tip was taken as the abscissa 0, and the transverse interval of 2 μm was taken as the measuring point. Seven positions were measured for each layer. The statistical results are presented in Fig. 5. The yellow column represents the thickness of Sample #1, and the green column represents the thickness of Sample #2. Both samples are thin in the middle and thick on the two sides, and the yellow column values are lower than the green column, that is, the thickness of the amorphous layer of Sample #1 is less than the thickness of the crystalline layer. Fig. 6 shows the thickness reduction T_r of the amorphous layer at the right middle position under the tip. The formula for calculating the thickness reduction T_r is [45]:

$$T_r = \Delta h / h_0 = (h_0 - h) / h_0 \tag{1}$$

Here, h_0 is the thickness of the amorphous layer before deformation, and h is the thickness of the amorphous layer after deformation. The thickness reduction of Sample #1 is always greater than Sample #2, which is consistent with the statistical results in Fig. 5. The experimental results show that highly-textured crystals are more beneficial for the thinning of amorphous layers. EDS results obtained in transmission electron microscope show that the elements have not diffused, as seen in Fig. 7. There are no shear steps and shear bands in the amorphous layer, indicating that the amorphous layer has a homogeneous flow.

We simulated deformation of four amorphous/crystalline bilayer structures under indentation, in which the crystalline layer is composed of single crystals using MD simulations. The indentations are aligned along the <111>, <220>, <112>, and <110> directions, respectively. The thickness of both amorphous and crystalline layers is 5 nm. The indenter is in direct contact with the crystalline layer. The crystalline layers were deformed first, and the stress was transferred to the amorphous layers, causing their deformation. In the deformed crystalline layer, two adjacent HCP layers represent a stacking fault. The simulation results show that the stacking faults and slip directions of crystalline layers with (111) orientation are almost parallel to the amorphous/crystalline interface, resulting in more dislocations generated by slip remaining in the crystalline layer, and only a small part of dislocations is

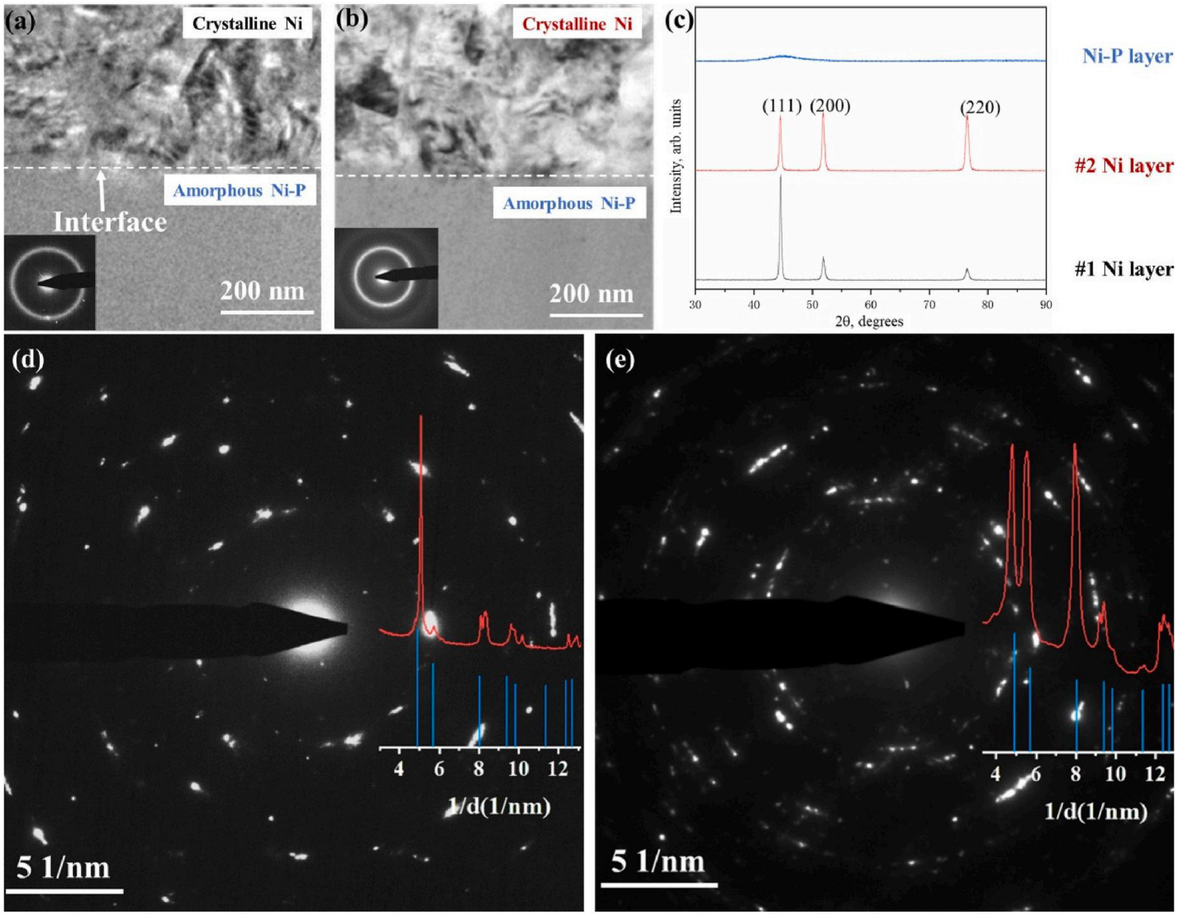

Fig. 3. TEM cross-section morphology of: (a) Sample #1 and (b) Sample #2. The inset shows the corresponding SAED patterns for the Ni–P layers. (c) XRD patterns of the Ni–P layer and two kinds of Ni layers. (d) and (e) are SAED patterns of the crystalline layers in (a) and (b), respectively.

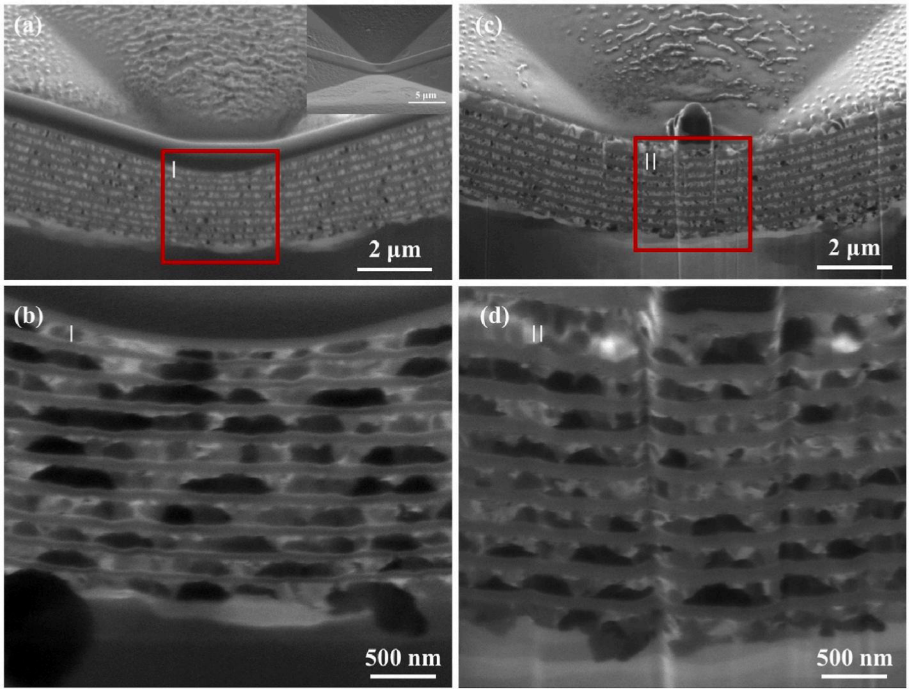

Fig. 4. Section morphology after 0.5 kgf Vickers indentation of (a) and (b) Sample #1, (c) and (d) Sample #2.

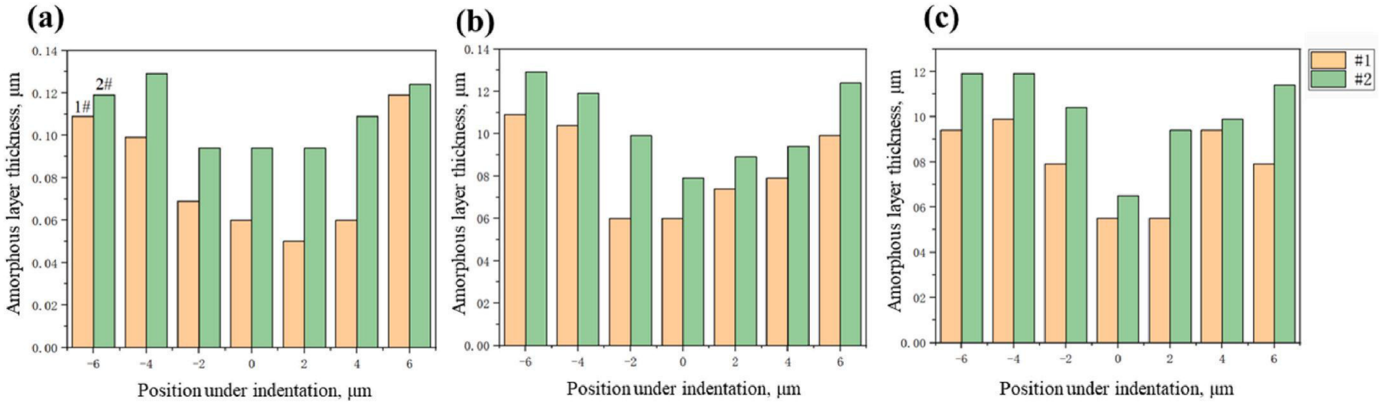

Fig. 5. Thickness statistics of the amorphous layer: (a), (b), and (c) represent three different layers of Samples #1 and #2. Here, 0 represents the center of indentation.

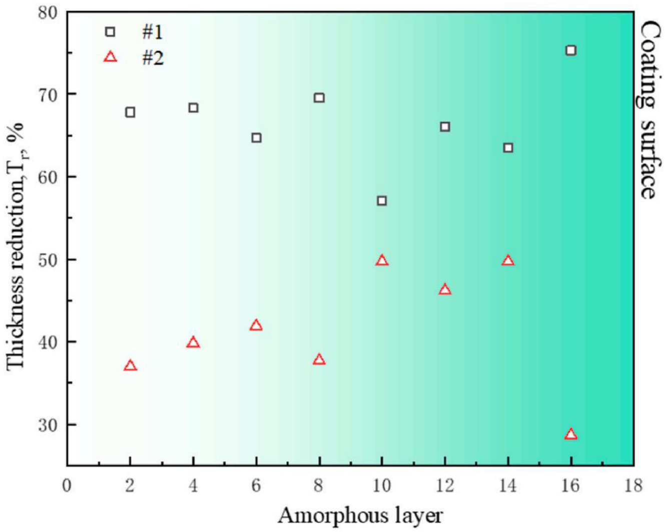

Fig. 6. Statistics of amorphous layer thickness reduction T_r under the indenter tip.

absorbed by the amorphous layer through the amorphous/crystalline interface, as seen in Fig. 8(a). For the other three crystalline layers, the stacking faults and slip direction intersect with the amorphous/crystalline interface so that the dislocation slip direction is inclined to the amorphous/crystalline interface, and the dislocation is more easily absorbed by the amorphous layer, as seen in Fig. 8(b–d). The thickness of crystalline and amorphous layers is thinner after deformation, which is consistent with the experimental results.

4. Discussion

The experimental results show that the thickness of the Ni–P amorphous layer in the amorphous/crystalline multilayer structure will decrease under pressure, and crystalline layers with the same thickness and different orientations will affect the thickness reduction of the amorphous layer. The thickness of each crystalline layer is thick enough, and is equal to the thickness of the amorphous layer in this experiment, reaching the submicron level, so there are no shear bands. It is well known that there are two basic deformation modes of amorphous materials [46]: homogeneous and inhomogeneous flow. In the homogeneous case, each volume element of the sample contributes to the strain. In the inhomogeneous case, the strain is limited to several very thin shear bands, and the basic physical process behind the inhomogeneous flow is the local softening of the material. In this work, the amorphous layer only has homogeneous flow without softening.

4.1. *Thickness reduction due to mutual constraints of amorphous and crystalline layers*

It is reported that the thickness of the amorphous layer decreases during rolling and tensile deformation. Donohue et al. [47] found that the shear band of nanoscale metallic glass is restrained by the ultra-thin crystalline layer. However, due to the limitation of layer thickness, both amorphous and crystalline layers are limited to the nanometer scale. The authors emphasized that the crystalline layer should also be thin enough to prevent dislocation accumulation. The stress concentration at the tip of stacking dislocation of the crystalline layer in a micron-scale layered structure will cause a shear band in the amorphous layer. On the other hand, the high flow strength of the crystalline layer is guaranteed. The thinning of the amorphous layer means that it has undergone plastic deformation. The free volume distributed in amorphous alloy, similar to vacancies in crystalline materials, is the portion of the volume around atoms that can be exchanged with neighboring atoms, resulting in annihilation under the action of the crystalline layer [46,48,49]. The density of atomic stacking in the amorphous layer becomes higher [50]. Lu et al. [45] found that the thickness of the micron amorphous layer decreased, but there was also inhomogeneous deformation of shear bands or cracks.

In this work the polycrystalline layer is Ni. For a crystalline layer, it has the following three characteristics. First, the grain size of nanocrystalline (NC) Ni is below 100 nm, and NC particles of this size lack the ability of strain harden, which is the key to maintaining the delocalized plastic strain [51]. Second, the FCC structure is the most ductile crystal structure, but the grain boundary strengthening of nanocrystals will lose ductility. Third, Ni has high stacking fault energy (SFE), $\gamma_{sf} = 128$ mJ/m^2 [52]. SFE is the main material property that determines the plasticity mechanism of FCC metals. According to the value of SFE, the plasticity mechanism of FCC metals can be divided into three types: dislocation slip ($\gamma_{sf} > 45$ mJ/m^2), mechanical twinning ($\gamma_{sf} = 15$–45 mJ/m^2), and strain-induced phase transformation ($\gamma_{sf} < 15$ mJ/m^2) [53]. Thus, the main deformation mechanism of Ni crystalline layers is dislocation slip. Here, due to the constraint and influence of the amorphous layers, the motion of dislocations in the crystalline layers slows down, and the interaction between dislocations is enhanced. As a result, the flow stress in the crystalline layers increases, and dislocation storage is promoted, which increases strain hardening of the crystalline layers while also possessing a certain degree of ductility. In this process, the crystalline layers will also be thinner [54].

Hence, amorphous/crystalline multilayer structures interact and constrain each other during deformation, which improves their strain-hardening ability. Strain-hardening ensures the delocalization of flow

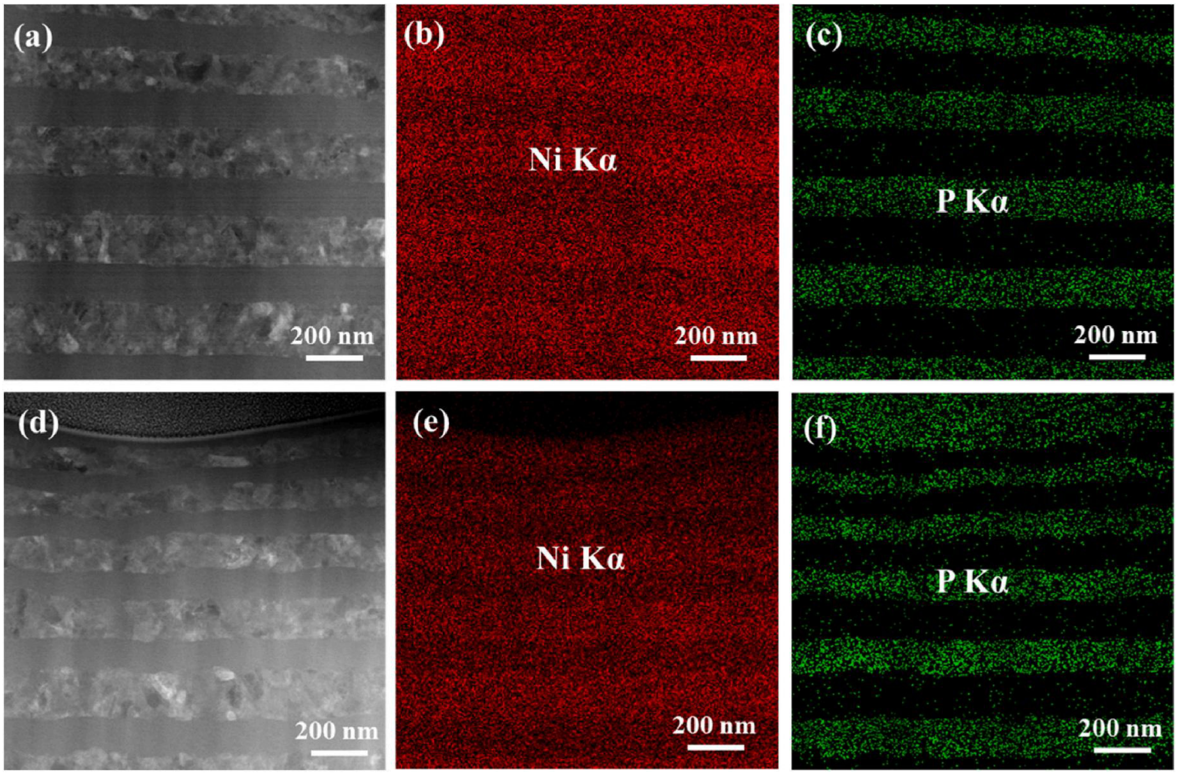

Fig. 7. EDS from transmission electron microscopy: (a) Cross-section morphology of Sample #1, (b) corresponding Ni distribution represented in red, (c) corresponding P distribution represented in green. (d) Cross-section morphology of Sample #2, (e) corresponding Ni distribution represented in red, (f) corresponding P distribution represented in green.

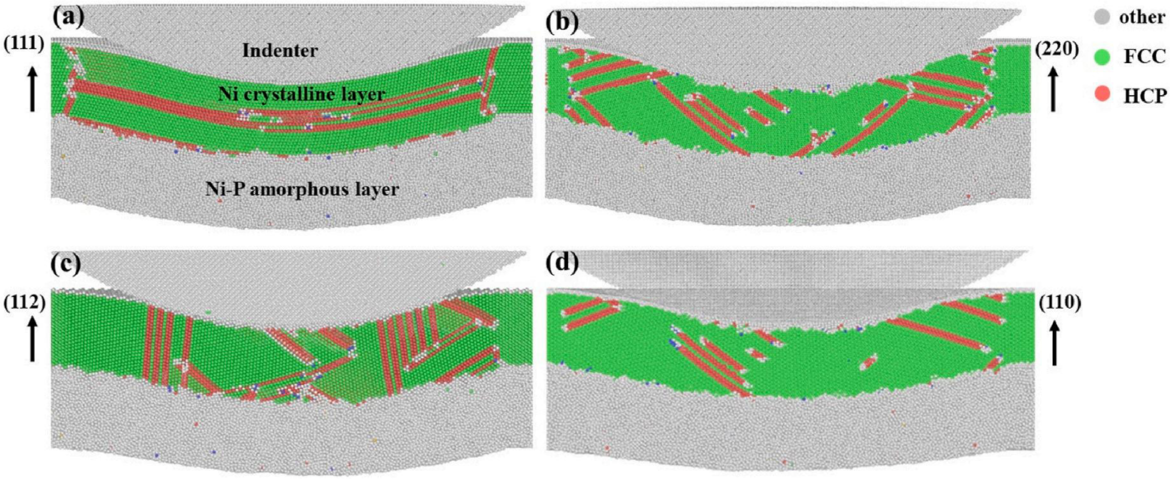

Fig. 8. MD simulation of the deformation of four kinds of amorphous/crystalline bilayer structures under indentation. The crystalline layers are: (a) (111), (b) (220), (c) (112), and (d) (110) oriented single crystals.

and improves the plasticity of the whole system. According to the energy conservation principle, the total energy of the whole system remains unchanged. The flow stress of the crystalline layer in the initial state is low when it is not deformed. After being pressed by the indenter, dislocations are introduced during the deformation process, then they interact and entangle, which increases the energy, leading to an increase in the flow stress [55,56]. However, the initial amorphous layer exhibits a certain flow stress due to the existence of free volume. STZs are generated during deformation, accompanied by energy consumption. Due to the crystalline layers absorbing kinetic energy of the immature shear bands of the amorphous layers [57], the shear bands cannot be started, and the amorphous layer undergoes structural relaxation. With the increase of atomic stacking, the free volumes begin to decrease and annihilate, the number of STZs decreases, the flow stress increases, and strain hardening is achieved. The corresponding deformation mechanism is shown in Fig. 9. Yellow represents movable atoms, and blue spheres represent less mobile atoms. It is easier for movable atoms to form STZs, and STZs are circled by dotted lines in Fig. 9. As the deformation proceeds, the atoms are stacked more closely, the number of yellow atoms is reduced, and the number of STZs circled by the dotted line decreases. The strain-hardening process of amorphous and crystalline layers is the opposite with completely different hardening

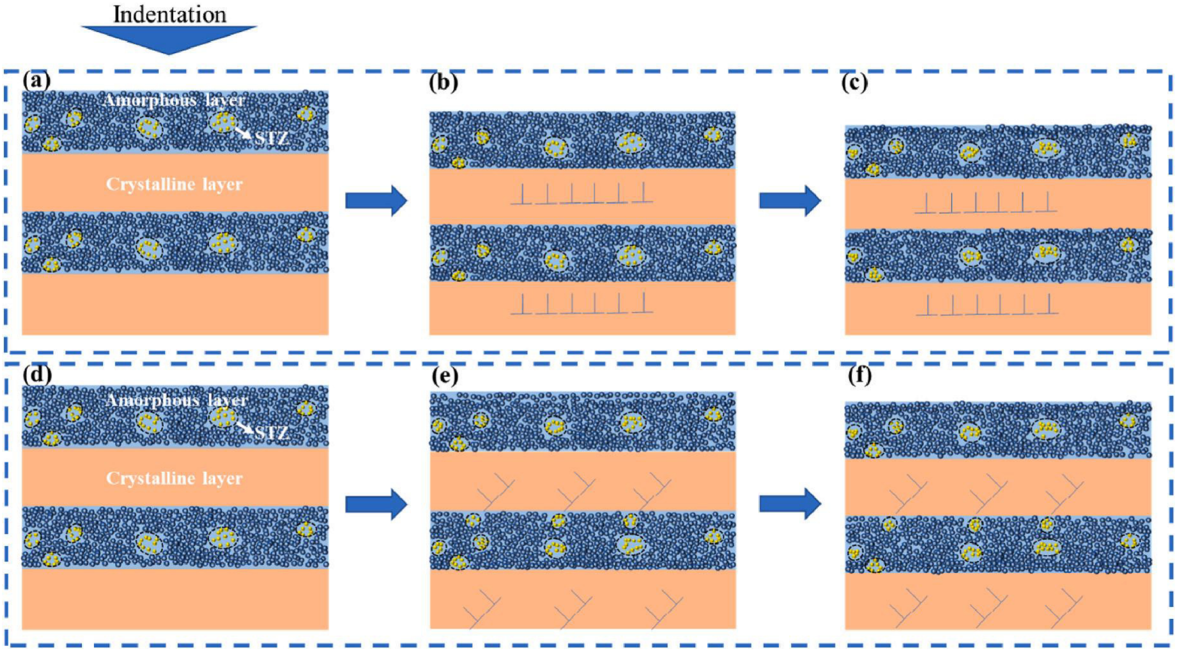

Fig. 9. (a–c) highly-textured (111) crystalline/amorphous multilayer, (d–f) untextured crystalline layers/amorphous multilayer deformation mechanism diagram. (a) and (d) are the same except for the crystalline layer texture. Yellow represents movable atoms, and blue spheres represent less mobile atoms.

mechanisms [58].

4.2. Effects of crystalline layers on the compression of amorphous layers

Based on the analysis of experimental results and MD simulations, the dislocation slip directions of the polycrystalline layer with high (111) texture are mainly parallel to the amorphous/crystalline interface, and dislocations are retained in the crystalline layer, as shown in Fig. 9(b and c). Literature shows that the dislocation density of FCC crystals with (111) orientation is higher. When dislocation density is high, dislocation slip is hindered. The higher the dislocation density, the higher the strength, and the strain-hardening ability will be stronger [59,60]. Therefore, the highly-textured (111) crystalline layer has a stronger strain-hardening ability. As the loading progresses, the crystalline layer becomes more and more difficult to deform, and the force of the indenter enters the amorphous layer, making the deformation of the amorphous layer more severe. Therefore, the free volume decreases and annihilates more, the flow is greater, and the atoms are packed more tightly. As a result, the compression of the amorphous layer is greater.

From the energy perspective, the work done by the indenter is converted into the energy of the amorphous/crystalline system. Based on the principle of energy conservation, the motion of dislocations in the crystalline layer increases its kinetic energy, so the energy increases more, and the energy of the adjacent amorphous layers decreases more. The lower the energy of the amorphous layers, the more the free volumes are reduced and annihilated, and the more the volume is densified, so the compression of the amorphous layers is greater.

For the crystalline layers in the untextured polycrystalline sample, the dislocation slip directions generated by the crystalline layer are not only parallel to the amorphous/crystalline layer interface but also more likely to intersect with the interface, resulting in more dislocations being absorbed by the amorphous layers. The absorbed dislocations activate the STZs at the amorphous layer near the amorphous/crystalline interface [61], as shown in Fig. 9(e). The STZs correspond to the free-volume-rich regions prone to shear transition [62], increasing the free volume of amorphous layers near the interface. At the same time, the free volume of other parts of the amorphous layer decreases and annihilates due to the pressure loading, as shown in Fig. 9(f). In general, the annihilation of free volume is less than the first sample, and the compression of the amorphous layer is smaller.

From the energy perspective, the energy of the amorphous layer increases due to the enrichment of a part of the free volume, but the pressure of the indenter finally reduces the energy of the amorphous layer. As a result, the energy reduction of the amorphous layers is less than amorphous layers constrained by (111) textured crystalline layers, and the free volume annihilation is less, so the compression of the amorphous layers is less.

In addition, after careful examination of the amorphous layers of the deformed samples, no nanocrystals were found as described in the literatures [25,63,64]. This indicates that no deformation-induced crystallization has occurred. The reason for this result is that the dislocations emitted by the soft Ni crystalline layer do not enter the amorphous layer with a strong stress field, but are absorbed by the amorphous layer at the interface. Although the STZs of the amorphous layer are triggered, it is not enough to induce atomic rearrangement of the amorphous layer [65].

5. Conclusions

In this work, the deformation mechanisms of the amorphous/crystalline multilayers with a submicron single layer thickness were studied using indentation experiments and MD simulations. Strain hardening of the amorphous layer to varying degrees was achieved by controlling the orientation of the crystalline layer. The main conclusions of this study are as follows.

(1) Amorphous/crystalline multilayers with a submicron single layer thickness can undergo plastic co-deformation under indentation, and the amorphous layer does not produce shear bands and achieves homogeneous flow. The thickness of both amorphous and crystalline layers decreased.
(2) The amorphous and crystalline layers interact and constrain each other during deformation. From the energy perspective, dislocation multiplication in crystalline layers leads to energy increase, while free volumes of amorphous layers decrease and annihilate, resulting in structural relaxation and energy decrease. Two

opposite processes fulfill their respective strain-hardening capabilities.

(3) The highly-textured (111) crystalline layer can make the amorphous layer thinner than the untextured crystalline layer. The essence of the former is that the strain-hardening ability of the textured crystalline layer is higher, the deformation of the corresponding amorphous layer is more intense, the free volume is reduced and annihilated more, the flow is greater, and the atom accumulation is more compact. The latter amorphous layer absorbs dislocations in the crystalline layer, activates STZs, increases the free volume of the amorphous near the interface, and the annihilation of the free volume is less than the former, so the former has a higher strain-hardening ability and greater compression.

CRediT authorship contribution statement

Hang Xu: Writing – original draft, Visualization, Investigation, Data curation. **Xiao-Ye Zhou:** Software. **Jingwen Qiu:** Validation. **Tao Guo:** Project administration, Methodology. **Kewei Gao:** Supervision, Resources. **Alex A. Volinsky:** Writing – review & editing. **Xiaolu Pang:** Writing – review & editing, Supervision, Funding acquisition.

Declaration of competing interest

The authors declare the following financial interests/personal relationships which may be considered as potential competing interests.

Xiaolu Pang reports financial support was provided by the National Natural Science Foundation of China. Jingwen Qiu reports financial support was provided by the science and technology innovation Program of Hunan Province. If there are other authors, they declare that they have no known competing financial interests or personal relationships that could have appeared to influence the work reported in this paper.

Data availability

The data that has been used is confidential.

Acknowledgments

This work was supported by the National Natural Science Foundation of China (51922002 and U21A2044) and the Science and Technology Innovation Program of the Hunan Province (2022RC4039).

References

[1] E. Axinte, Metallic glasses from “alchemy” to pure science: present and future of design, processing and applications of glassy metals, Mater. Des. 35 (2012) 518–556.
[2] W.H. Wang, The elastic properties, elastic models and elastic perspectives of metallic glasses, Prog. Mater. Sci. 57 (3) (2012) 487–656.
[3] S. Sohrabi, J. Fu, L. Li, Y. Zhang, X. Li, F. Sun, J. Ma, W.H. Wang, Manufacturing of metallic glass components: processes, structures and properties, Prog. Mater. Sci. 144 (2024).
[4] J. Schroers, BULK metallic glasses, Phys. Today 66 (2) (2013) 32–37.
[5] M. Telford, The case for bulk metallic glass, Mater, Today Off. 7 (3) (2004) 36–43.
[6] D. Jang, J.R. Greer, Transition from a strong-yet-brittle to a stronger-and-ductile state by size reduction of metallic glasses, Nat. Mater. 9 (3) (2010) 215–219.
[7] C. Suryanarayana, Mechanical behavior of emerging materials, Mater. Today 15 (11) (2012) 486–498.
[8] R. Alben, J.J. Becker, M.C. Chi, Random anisotropy in amorphous ferromagnets, J. Appl. Phys. 49 (3) (1978) 1653–1658.
[9] Y.-C. Lin, Y.-C. Tsai, T. Ono, P. Liu, M. Esashi, T. Gessner, M. Chen, Metallic glass as a mechanical material for microscanners, Adv. Funct. Mater. 25 (35) (2015) 5677–5682.
[10] J.-Q. Wang, Y.-H. Liu, M.-W. Chen, G.-Q. Xie, D.V. Louzguine-Luzgin, A. Inoue, J. H. Perepezko, Rapid degradation of azo dye by Fe-based metallic glass powder, Adv. Funct. Mater. 22 (12) (2012) 2567–2570.
[11] D.C. Hofmann, R. Polit-Casillas, S.N. Roberts, J.-P. Borgonia, R.P. Dillon, E. Hilgemann, J. Kolodziejska, L. Montemayor, J.-o. Suh, A. Hoff, K. Carpenter, A. Parness, W.L. Johnson, A. Kennett, B. Wilcox, Castable bulk metallic glass strain wave gears: towards decreasing the cost of high-performance robotics, Sci. Rep. 6 (2016).
[12] A. Grimberg, H. Baur, P. Bochsler, F. Buehler, D.S. Burnett, C.C. Hays, V.S. Heber, A.J.G. Jurewicz, R. Wieler, Solar wind neon from Genesis: implications for the lunar noble gas record, Science 314 (5802) (2006) 1133–1135.
[13] Y.M. Wang, J. Li, A.V. Hamza, T.W. Barbee, Ductile crystalline-amorphous nanolaminates, Proc. Natl. Acad. Sci. U.S.A. 104 (27) (2007) 11155–11160.
[14] H.S. Chou, X.H. Du, C.J. Lee, J.C. Huang, Enhanced mechanical properties of multilayered micropillars of amorphous ZrCuTi and nanocrystalline Ta layers, Intermetallics 19 (7) (2011) 1047–1051.
[15] J.Y. Zhang, G. Liu, S.Y. Lei, J.J. Niu, J. Sun, Transition from homogeneous-like to shear-band deformation in nanolayered crystalline Cu/amorphous Cu-Zr micropillars: intrinsic vs. extrinsic size effect, Acta Mater. 60 (20) (2012) 7183–7196.
[16] W. Guo, E.A. Jagle, P.P. Choi, J.H. Yao, A. Kostka, J.M. Schneider, D. Raabe, Shear-induced mixing governs codeformation of crystalline-amorphous nanolaminates, Phys. Rev. Lett. 113 (3) (2014) 5.
[17] Y. Cui, O.T. Abad, F. Wang, P. Huang, T.J. Lu, K.W. Xu, J. Wang, Plastic deformation modes of CuZr/Cu multilayers, Sci. Rep. 6 (2016).
[18] J. Zhu, C. Gu, K.W. Xu, P. Huang, F. Wang, T.J. Lu, Effects of size and amorphous layer structure on the strength and plasticity of Cu/CuZr nanolaminates, Mater. Sci. Eng. A-Struct. Mater. Prop. Microstruct. Process. 738 (2018) 219–228.
[19] X.Y. Cuan, J. Pan, R.Q. Cao, Y. Lin, J.H. Yao, Y.X. Wang, Y. Li, Effect of amorphous layer thickness on the tensile behavior of bulk-sized amorphous Ni-P/crystalline Ni laminates, Mater. Lett. 218 (2018) 150–153.
[20] Y.F. Zhao, B. Chen, Y.Q. Wang, J.Y. Zhang, S.Z. Li, K. Wu, G. Liu, J. Sun, Size-dependent microstructural evolution and mechanical properties of crystalline/amorphous high-entropy alloy nanostructured multilayers: Cu/FeCoCrNiBSi vs Ni/FeCoCrNiBSi, Acta Mater. 246 (2023) 118706.
[21] K.E. Avila, V.H. Vardanyan, S. Kuchemann, H.M. Urbassek, Response of an amorphous/crystalline interface to nanoindentation: an atomistic study, Appl. Surf. Sci. 551 (2021).
[22] T. Yue, Y.Q. Wang, J.Y. Zhang, K. Wu, G. Li, J. Kuang, G. Liu, J. Sun, Unraveling the discrepancies in size dependence of hardness and thermal stability in crystalline/amorphous nanostructured multilayers: Cu/Cu-Ti vs. Cu/HfO2, Nanoscale 10 (29) (2018) 14331–14341.
[23] T. Mueller, A. Bachmaier, R. Konetschnik, T. Schoeberl, R. Pippan, Mechanical properties of electrodeposited amorphous/crystalline multilayer structures in the Fe-P system, Mater. Sci. Eng. A-Struct. Mater. Prop. Microstruct. Process. 715 (2018) 83–91.
[24] G. Wu, C. Liu, A. Brognara, M. Ghidelli, Y. Bao, S. Liu, X. Wu, W. Xia, H. Zhao, J. Rao, D. Ponge, V. Devulapalli, W. Lu, G. Dehm, D. Raabe, Z. Li, Symbiotic crystal-glass alloys via dynamic chemical partitioning, Mater. Today 51 (2021) 6–12.
[25] Y.Q. Wang, K. Wu, J.Y. Zhang, G. Liu, J. Sun, Probing the size- and constituent-mediated mechanical properties and deformation behavior in crystalline/amorphous nanolaminates, Nanoscale 10 (46) (2018) 21827–21841.
[26] W. Guo, E. Jägle, J. Yao, V. Maier, S. Korte-Kerzel, J.M. Schneider, D. Raabe, Intrinsic and extrinsic size effects in the deformation of amorphous CuZr/nanocrystalline Cu nanolaminates, Acta Mater. 80 (2014) 94–106.
[27] Y.Q. Wang, J.Y. Zhang, X.Q. Liang, K. Wu, G. Liu, J. Sun, Size- and constituent-dependent deformation mechanisms and strain rate sensitivity in nanolaminated crystalline Cu/amorphous Cu-Zr films, Acta Mater. 95 (2015) 132–144.
[28] W. Guo, J. Yao, E.A. Jaegle, P.-P. Choi, M. Herbig, J.M. Schneider, D. Raabe, Deformation induced alloying in crystalline - metallic glass nano-composites, Mater. Sci. Eng. A-Struct. Mater. Prop. Microstruct. Process. 628 (2015) 269–280.
[29] H.Y. Song, M. Wang, Q. Deng, Y.L. Li, Deformation mode transitions in Cu50Zr50 amorphous/Cu crystalline nanomultilayer: a molecular dynamics study, J. Non-Cryst. Solids 490 (2018) 13–21.
[30] Z.L. Pan, T.J. Rupert, Amorphous intergranular films as toughening structural features, Acta Mater. 89 (2015) 205–214.
[31] S. Pal, K.V. Reddy, C. Deng, On the role of Cu-Zr amorphous intergranular films on crack growth retardation in nanocrystalline Cu during monotonic and cyclic loading conditions, Comput. Mater. Sci. 169 (2019).
[32] H.F. Tan, B. Zhang, Y.K. Yang, X.F. Zhu, G.P. Zhang, Fracture behavior of sandwich-structured metal/amorphous alloy/metal composites, Mater. Des. 90 (2016) 60–65.
[33] H.Y. Song, J.L. Dai, M.R. An, M.X. Xiao, Y.L. Li, Atomic simulation of deformation behavior of dual-phase crystalline/amorphous Mg/Mg-Al nanolaminates, Comput. Mater. Sci. 165 (2019) 88–95.
[34] E. Alishahi, C. Deng, Orientation dependent plasticity of metallic amorphous-crystalline interface, Comput. Mater. Sci. 141 (2018) 375–387.
[35] L. Qian, W. Yang, J. Luo, Y. Wang, K.C. Chan, X.-S. Yang, Amorphous thickness-dependent strengthening-softening transition in crystalline-amorphous nanocomposites, Nano Lett. 23 (23) (2023) 11288–11296.
[36] W.-P. Wu, D. Sopu, J. Eckert, Molecular dynamics study of the nanoindentation behavior of Cu64Zr36/Cu amorphous/crystalline nanolaminate composites, Materials 14 (11) (2021).
[37] F. Ren, S. Zhao, W. Li, B. Tian, L. Yin, A.A. Volinsky, Theoretical explanation of Ag/Cu and Cu/Ni nanoscale multilayers softening, Mater. Lett. 65 (1) (2011) 119–121.
[38] J. Pridans, J.C. Bilello, Plastic constraint as a mechanism for film strengthening, Acta Metall. 20 (12) (1972) 1339–1346.
[39] H.W. Sheng, E. Ma, M.J. Kramer, Relating dynamic properties to atomic structure in metallic glasses, Jom 64 (7) (2012) 856–881.

[40] A. Stukowski, Visualization and analysis of atomistic simulation data with OVITO-the Open Visualization Tool, Model. Simulat. Mater. Sci. Eng. 18 (6) (2010) 2154–2162.

[41] A. Stukowski, K. Albe, Extracting dislocations and non-dislocation crystal defects from atomistic simulation data, Model. Simulat. Mater. Sci. Eng. 18 (8) (2010) 085001.

[42] A.M. Pillai, A. Rajendra, A.K. Sharma, Electrodeposited nickel-phosphorous (Ni-P) alloy coating: an in-depth study of its preparation, properties, and structural transitions, J. Coating Technol. Res. 9 (6) (2012) 785–797.

[43] J. Chen, Q. Meng, S. Zhang, K. Chong, W. Zhao, Y. Zou, Insights into corrosion resistance enhancement of nickel–phosphorus metallic glass in acid environment by the incorporation of copper, Vacuum 195 (2022) 110705.

[44] H. Shi, M. Luo, W. Wang, ElectronDiffraction tools, a DigitalMicrograph package for electron diffraction analysis, Comput. Phys. Commun. 243 (2019) 166–173.

[45] X.L. Lu, Y. Li, L. Lu, Co-existence of homogeneous flow and localized plastic deformation in tension of amorphous Ni–P films on ductile substrate, Acta Mater. 106 (2016) 182–192.

[46] F. Spaepen, A microscopic mechanism for steady state inhomogeneous flow in metallic glasses, Acta Metall. 25 (4) (1977) 407–415.

[47] A. Donohue, F. Spaepen, R.G. Hoagland, A. Misra, Suppression of the shear band instability during plastic flow of nanometer-scale confined metallic glasses, Appl. Phys. Lett. 91 (24) (2007).

[48] P. Murali, U. Ramamurty, Embrittlement of a bulk metallic glass due to sub-Tg annealing, Acta Mater. 53 (5) (2005) 1467–1478.

[49] L.Z. Zhao, R.J. Xue, Z.G. Zhu, Z. Lu, E. Axinte, W.H. Wang, H.Y. Bai, Evaluation of flow units and free volumes in metallic glasses, J. Appl. Phys. 116 (10) (2014).

[50] C. Wang, Z.Z. Yang, T. Ma, Y.T. Sun, Y.Y. Yin, Y. Gong, L. Gu, P. Wen, P.W. Zhu, Y. W. Long, X.H. Yu, C.Q. Jin, W.H. Wang, H.Y. Bai, High stored energy of metallic glasses induced by high pressure, Appl. Phys. Lett. 110 (11) (2017).

[51] K. Lu, Stabilizing nanostructures in metals using grain and twin boundary architectures, Nat. Rev. Mater. 1 (5) (2016).

[52] D.C. Bufford, Y.M. Wang, Y. Liu, L. Lu, Synthesis and microstructure of electrodeposited and sputtered nanotwinned face-centered-cubic metals, MRS Bull. 41 (4) (2016) 286–291.

[53] B.C. De Cooman, Y. Estrin, S.K. Kim, Twinning-induced plasticity (TWIP) steels, Acta Mater. 142 (2018) 283–362.

[54] H. Li, H.X. Zong, S.Z. Li, S.B. Jin, Y. Chen, M.J. Cabral, B. Chen, Q.W. Huang, Y. Chen, Y. Ren, K.Y. Yu, S. Han, X.D. Ding, G. Sha, J.S. Lian, X.Z. Liao, E. Ma, J. Sun, Uniting tensile ductility with ultrahigh strength via composition undulation, Nature 604 (7905) (2022), 273-+.

[55] W. Zielinski, H. Huang, W.W. Gerberich, Microscopy and microindentation mechanics of single crystal Fe−3 wt. % Si: Part II. TEM of the indentation plastic zone, J. Mater. Res. 8 (6) (1993) 1300–1310.

[56] W. Zielinski, M.J. Lii, W.W. Gerberich, Crack-tip dislocation emission arrangements for equilibrium —I. In situ TEM observations of Fe2wt%Si, Acta Metall. Mater. 40 (11) (1992) 2861–2871.

[57] M.C. Liu, C.J. Lee, Y.H. Lai, J.C. Huang, Microscale deformation behavior of amorphous/nanocrystalline multilayered pillars, Thin Solid Films 518 (24) (2010) 7295–7299.

[58] J. Pan, Y.P. Ivanov, W.H. Zhou, Y. Li, A.L. Greer, Strain-hardening and suppression of shear-banding in rejuvenated bulk metallic glass, Nature 578 (7796) (2020) 559–562.

[59] Q. Yin, Y.D. Lian, Z.X. Wen, H.Q. Pei, J.D. Wang, Z.F. Yue, Atomic simulation of the effect of orientation on tensile/compressive properties in nickel-based single crystal superalloys, J. Alloys Compd. 893 (2022).

[60] L. Liu, J. Meng, J. Liu, T. Jin, X. Sun, H. Zhang, Effects of crystal orientations on the cyclic deformation behavior in the low cycle fatigue of a single crystal nickel-base superalloy, Mater. Des. 131 (2017) 441–449.

[61] P. Thanh, J. Rigelesaiyin, Y. Chen, A. Bastawros, L. Xiong, Metallic glass instability induced by the continuous dislocation absorption at an amorphous/crystalline interface, Acta Mater. 189 (2020) 10–24.

[62] A.S. Argon, M.J. Demkowicz, What can plasticity of amorphous silicon tell us about plasticity of metallic glasses? Metall. Mater. Trans. A 39 (8) (2008) 1762–1778.

[63] L. Zhang, S. Su, W. Fu, J. Sun, Z. Ning, A.H.W. Ngan, Y. Huang, Strain-induced structural evolution of interphase interfaces in CuZr-based metallic-glass composite reinforced by B2 crystalline phase, Compos. Pt. B-Eng. 258 (2023).

[64] J.Y. Zhang, G. Liu, J. Sun, Self-toughening crystalline Cu/amorphous Cu-Zr nanolaminates: deformation-induced devitrification, Acta Mater. 66 (2014) 22–31.

[65] B. Cheng, J.R. Trelewicz, Mechanistic coupling of dislocation and shear transformation zone plasticity in crystalline-amorphous nanolaminates, Acta Mater. 117 (2016) 293–305.